LASER & PHOTONICS REVIEWS
www.lpr-journal.org

Large-Area, High-Numerical-Aperture, Freeform Metasurfaces

*You Zhou, Chenkai Mao, Erez Gershnabel, Mingkun Chen, and Jonathan A. Fan**

Nanophotonic devices are optical platforms capable of unprecedented wavefront control. To push the limits of experimental device performance, scalable design methodologies that combine the simplicity and fabricability of conventional design paradigms with the extended capabilities of freeform optimization are required. A novel gradient-based design framework for large-area freeform metasurfaces is introduced in which nonlocal interactions between simply shaped nanostructures, placed on an irregular lattice, are tailored to produce high-order hybridized modes that support customizable large-angle scattering profiles. Utilizing this approach, multifunctional super-dispersive metalenses are designed and experimentally demonstrated. The approach to high-numerical-aperture radial metalenses capable of diffraction limited focusing and the generation of donut-shaped point spread functions is also extended. It is anticipated that these concepts will have utility in super-resolution microscopy, particle trapping, additive manufacturing, and metrology applications that require ultra-high numerical apertures.

1. Introduction

Recent advancements in wavefront shaping using nanostructured materials have gained significant importance across a wide range of scientific and technological domains, including communications[1] sensing, imaging, and optical computing.[2,3] Through proper design of subwavelength-scale building blocks, nanophotonic devices can be realized to serve as compact, multifunctional elements[4,5] for lensing,[6–9] polarimetry[10–12] and holography,[13,14] making them attractive alternatives to conventional optics. Nonlocal flat optics supporting tailored long-range interaction have also been explored to achieve large angular and spectral selectivity,[15–17] leading to applications of wavefront selection,[18] image differentiation,[3] and phase contrast microscopy.[19,20] The vast majority of these concepts utilize conventional design principles based on libraries of simple and physically intuitive nanoscale elements, which are straightforward to implement into large-scale devices with minimal computational cost.[21,22] However, this approach is constrained by a limited design landscape that is often insufficient for the realization of complex devices, including those with high efficiency, large numerical apertures (NAs), multiplexed responses, and multi-wavelength operation.

Alternatively, inverse design based on freeform topology optimization can significantly expand the design landscape of nanophotonics. These strategies treat the design problem as the maximization of a desired Figure of Merit (FOM), and they employ computational algorithms to iteratively explore the design space with the aim of maximizing the FOM. Leading algorithms, such as the adjoint variables method,[23,24] are gradient-based optimizers that utilize reciprocity symmetries within Maxwell's equations to efficiently modify every dielectric voxel within the simulation domain in a manner that enhances the FOM. These computational approaches enable the utilization of non-trivial light-matter interactions including near-field coupling between elements, higher order modes within elements, and multiple scattering dynamics,[17,25] which can lead to freeform metagratings,[25,26] birefringent elements,[27] metalenses,[28–31] disordered metasurfaces[32] 3D meta-optics[33] and on-chip photonic devices[34,35] with new and enhanced capabilities. However, the complex geometries resulting from this freeform design process present significant challenges in nanofabrication[36] and are often sensitive to non-systematic perturbations such as surface roughness. Numerous strategies to enhance the robustness of freeform designs have been proposed, including the increase of voxel dimensions,[34,37] implementation of threshold filters,[38–40] and penalization of layouts that violate predefined design constraints,[36,41] but they have limited efficacy in practice. Furthermore, previous studies typically involve the design of whole devices at once,[29,42] leading to challenges for large-scale optimization due to extensive computation resources that are required.

In this study, we introduce a strategy for designing large-area freeform metasurfaces in which near-field interactions between simple nanoscale elements are leveraged to enable novel wavefront engineering regimes such as high-performance,

Y. Zhou, C. Mao, E. Gershnabel, M. Chen, J. A. Fan
Department of Electrical Engineering
Stanford University
Stanford, CA 94305, USA
E-mail: jonfan@stanford.edu
E. Gershnabel
Israel Aerospace Industries
Ben Gurion International Airport
Lod 7010000, Israel

The ORCID identification number(s) for the author(s) of this article can be found under https://doi.org/10.1002/lpor.202300988

DOI: 10.1002/lpor.202300988

 © 2024 Wiley-VCH GmbH

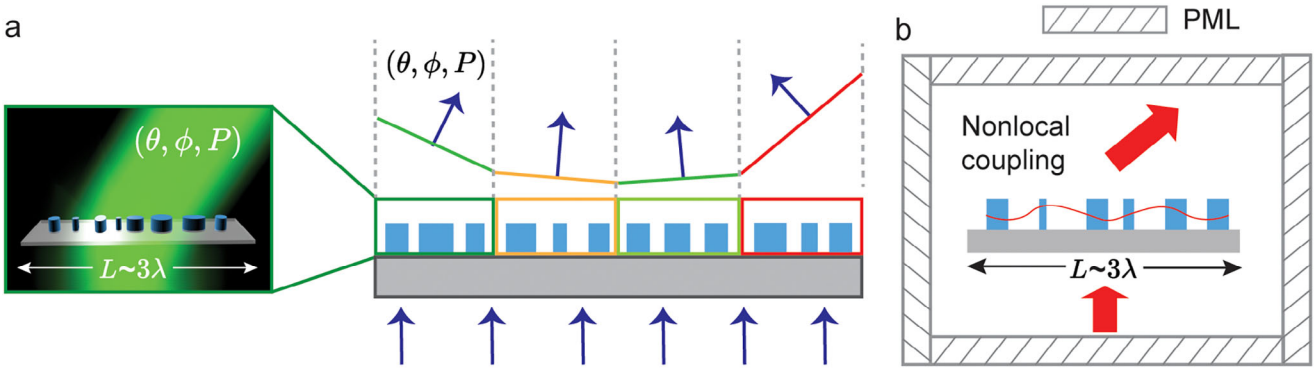

Figure 1. Large-area, reparameterized, freeform metasurfaces. a) Schematic of the design concept. The wavefront profile of a large-scale device is sampled into a series of wavelength-scale, linear scatters. Each scatter consists of nanostructures with simple geometric layouts, which effectively redirects light at a particular angle, phase and polarization with high efficiency (inset on the left). b) A schematic of the design concept for creating a wavelength-scale scatterer capable of deflecting light at a large angle. To ensure local response of the scatter, the deflector is designed in an open space surrounded by perfectly matched layers (PMLs). The nonlocal interaction between adjacent nanostructures plays a crucial role in facilitating strong scattering in the desired direction.

high-NA optics. To ensure the computational tractability and scalability of the concept, the desired wavefront profile is subdivided into wavelength-scale "super-pixel" regions, within which gradient-based optimization is used to tailor the geometry, position, and orientation of nanoscale elements. The concept combines ease of manufacturing from conventional design methods, utilization of extended design landscapes from freeform optimization, and enforcement of hard minimum feature size constraints, thereby providing a balance between metasurface design, fabricability, and performance.

2. Results

2.1. Design Principle

A schematic of the design concept is shown in **Figure 1a** and shows the wavefront profile of the full device partitioned into wavelength-scale super-pixels.[30] Each super-pixel is specified to function as a scatterer that effectively redirects an incident light beam to a particular angle, phase, and polarization with high efficiency (Figure 1a, inset). By subdividing the full wavefront profile in this manner, different super-pixels can be optimized in parallel, dramatically reducing the total computational cost compared to the optimization of the entire device in a single step. Figure 1b presents a schematic that illustrates the design concept for a super-pixel capable of performing directional beam scattering. The device is surrounded by perfectly matched layers (PMLs) and modeled using full-wave simulations without approximations. The nanoscale elements comprise elliptical silicon (Si) posts with tailorable axes, angles, and positions.

Our utilization of super-pixel scatterers leads to the approximation of the desired phase profile as a series of linear segments, which can introduce artifacts into the device wavefront response. To minimize this impact of linearization, we describe the curvilinear phase profile using a 2nd-order Taylor series expansion:

$$\phi(x) = \phi(x_0) + \phi'(x_0)(x - x_0) + \frac{1}{2}\phi''(x_0)(x - x_0)^2 \quad (1)$$

Given a section of length d at position x_0, we further derive the condition for achieving minimal root-mean-square (RMS) wavefront error[30]:

$$\varepsilon_{rms} = \frac{1}{12\sqrt{5}}\phi''(x_0)\, d^2 \quad (2)$$

For the majority of applications, linearizing the phase profiles with 3λ-wide segments has a negligible impact on the overall performance. To mitigate coupling effects during the stitching process, we impose a gap of $\approx 0.1\lambda$ to separate the structures between sections. The performance of the stitched device is further evaluated to ensure the absence of spurious diffraction and discontinuities between neighboring sections.

To ensure ease of fabrication in a manner that streamlines with gradient-based freeform optimization, we utilize a reparameterization scheme in which the dimensions and positions of nanoscale elements within a super-pixel are represented as latent variables that can be transformed into physical layouts using analytic expressions.[43] In this manner, minimum feature size and gap constraints are hard coded into the element representations. In addition, the reparameterization process regularizes the design process by reducing the dimensionality of the design space and eliminating device layouts that violate minimum size constraints, thereby enhancing optimization performance. Furthermore, the engineering of latent variables facilitates more directed search in the physical optimization landscape, resulting in designs with fewer local optima.[44] A detailed discussion of our reparameterization formalism and the analytic functions used to describe elliptically-shaped nanopost elements with size constraints is in the Section S1 (Supporting Information). Our reparameterization scheme can be readily incorporated into gradient-based topology optimization algorithms based on the adjoint variables method, as shown in the computational graph in **Figure 2a**. As the reparameterization process is fully analytic and differentiable, the gradients of FOMs with respect to the latent variables can be obtained through backpropagation and the chain rule. The proposed framework provides a scalable solution to designing

© 2024 Wiley-VCH GmbH

18638899, 0, Downloaded from https://onlinelibrary.wiley.com/doi/10.1002/lpor.202300988 by Stanford University, Wiley Online Library on [31/03/2024]. See the Terms and Conditions (https://onlinelibrary.wiley.com/terms-and-conditions) on Wiley Online Library for rules of use; OA articles are governed by the applicable Creative Commons License

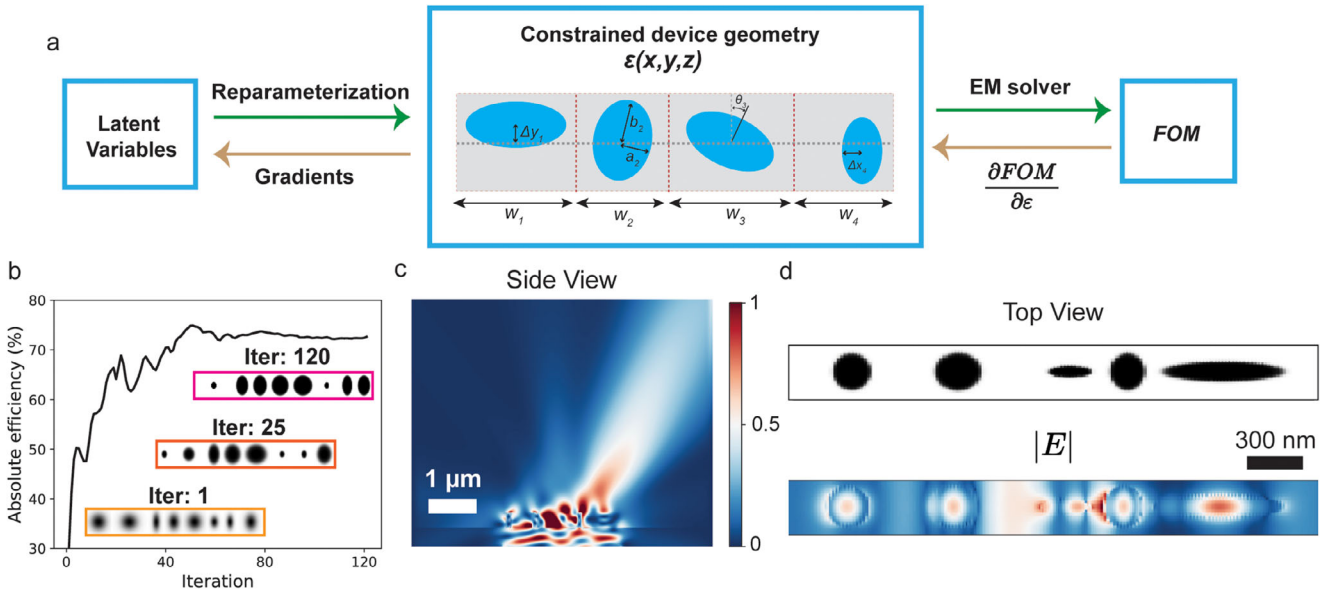

Figure 2. 3D reparameterization concept for designing aperiodic scatters. a) Computational graph representation of the reparameterization process. b) The optimization trajectory for a representative high-performance device consisting of an ensemble of simple geometric features. c) Side view of the electric field distributions of an optimized deflector. d) Top view of an aperiodic deflector and its electric field distribution, showing strong near-field coupling between adjacent nanostructures.

large-scale devices, in contrast to previous studies[29,33,35] in which the whole devices are designed at once. Additionally, it also enables a rapid global search in the non-convex design landscape, allowing to achieve performances that exceed that of direct large-scale optimization (further details of quantitative analysis can be found in Section S2, Supporting Information).

We use our reparameterized adjoint variables algorithm to design multifunctional super-pixels based on Si, which is an ideal material choice for metasurfaces due to its high-index, low-loss properties. We consider 350 nm-thick elements with minimum feature and gap sizes of 70 nm, an operating wavelength of 900 nm, and 3λ-wide super-pixel widths. The optimization trajectory for a representative high-performance device is shown in Figure 2b. The aperiodic scatter begins as a set of randomize dielectric posts with various grayscale values that consist of a mix of air void and high-index materials, and through the optimization process, the device evolves into a binary structure consisting of an array of elliptical posts. Figure 2c shows an intensity plot of an optimized deflector, indicating that 75% of the power is scattered toward a singular direction within the device aperture. The top view of the designed permittivity profile and electric field distribution (Figure 2d) reveal significant near-field coupling between adjacent nanostructures despite the similar simplicity in the geometries, indicating that nonlocal coupling plays a crucial role in facilitating strong scattering in the desired direction (see detailed results of a similar deflector designed based on conventional phase arrays in Figure S4, Supporting Information).

2.2. Polarization Multiplexed Super Off-Axis Focusing

To illustrate the capabilities of our freeform super-pixel design approach, we design and evaluate various embodiments of high-NA, multifunctional metasurfaces. First, we design and experimentally demonstrate a multifunctional metadevice capable of focusing light at extremely large off-axis positions, with independently specified focusing displacements for transverse electric (TE) and transverse magnetic (TM) polarizations (**Figure 3a**). Such off-axis focusing is well-known for its highly dispersive properties, with spectral resolution dependent on the scale of off-axis displacement.[45] The extreme dispersion achieved by this design method makes it suitable for applications such as a compact spectrometer for applications such as sensing and hyperspectral imaging.[46] The functionality demonstrated by the device is different from previous methods relying on locally engineered birefringent elements,[47,48] as it requires non-local optical interactions to enable independent and extremely large-angle wavefront manipulation for the two polarizations. The device is 81 μm (90 λ) wide and focuses light to horizontal positions of −121.5 and 121.5 μm for TE and TM polarization, respectively. Despite the symmetric off-axis distances, asymmetric focusing with different horizontal positions can also be achieved (see details of the design and full-wave simulation in Section S3, Supporting Information). To identify high-performing super-pixels, we perform twenty-five optimizations with randomly generated initial dielectric distributions for each super-pixel and select designs with the highest balanced metrics, taking into account efficiency for deflection at the desired scattering angle and the phase that most closely aligns with the phase target. The same selection process is employed for the design of all other devices. To validate the optical performance of the final optimized device, we perform full-wave simulation of the device using an open-source finite-difference time-domain (FDTD) solver, MEEP.[49] The full-wave simulations of the axial intensity distributions for the TE and TM polarizations (Figure 3b,c) demonstrate efficient off-axis focusing with minimal spurious diffraction.

© 2024 Wiley-VCH GmbH

18638899, 0, Downloaded from https://onlinelibrary.wiley.com/doi/10.1002/lpor.202300988 by Stanford University, Wiley Online Library on [31/03/2024]. See the Terms and Conditions (https://onlinelibrary.wiley.com/terms-and-conditions) on Wiley Online Library for rules of use; OA articles are governed by the applicable Creative Commons License

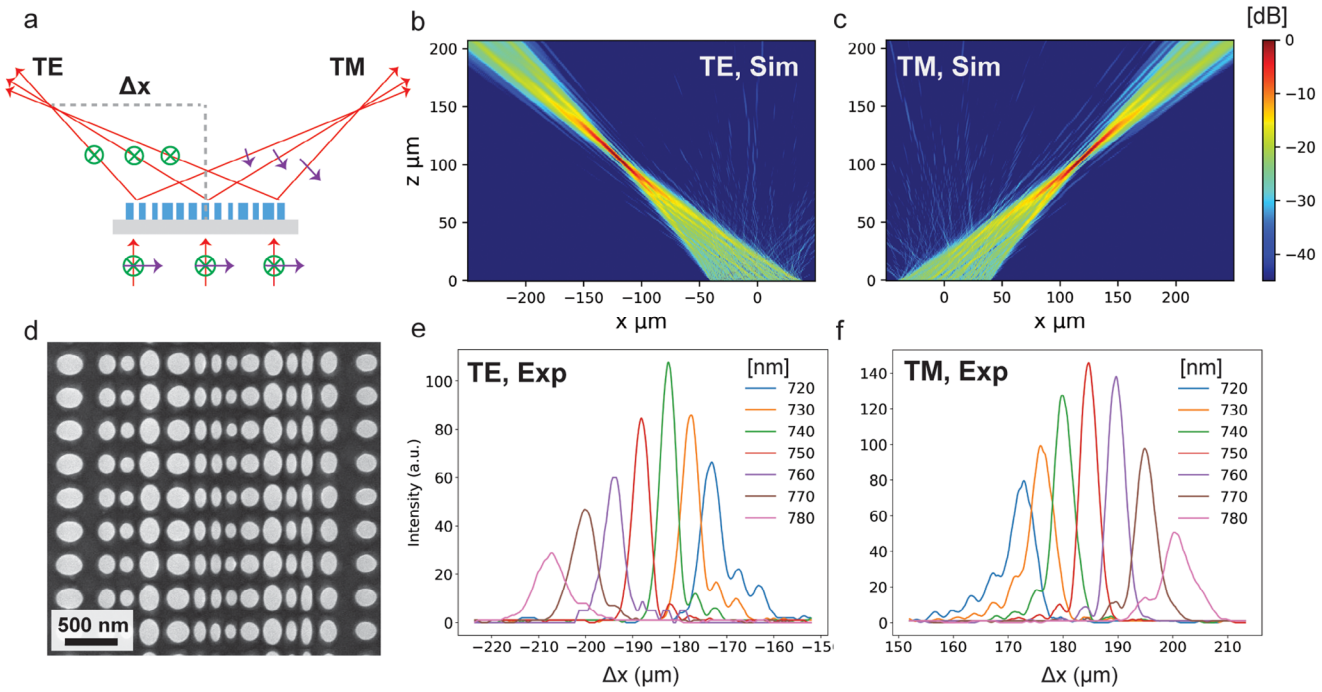

Figure 3. Polarization multiplexed super off-axis focusing. a) A schematic of the polarization multiplexed metalens designed to focus light at extremely large off-axis displacements, with independently specified focusing displacements for transverse electric (TE) and transverse magnetic (TM) polarizations. b,c) Full-wave simulations of the axial intensity distributions for TE b) and TM c) polarizations. d) Scanning electron microscope (SEM) image of the fabricated device. Experimental 1D horizontal cut of the focal spots at different wavelengths for e) TE and f) TM polarizations.

To further validate our design experimentally, we design and fabricate a 135 µm-wide polysilicon device using standard electron beam lithography and reactive ion etching methods. The scanning electron microscope (SEM) image is shown in Figure 3d and displays well-defined elliptical nanoposts consistent with the design. To characterize the device, we use a supercontinuum laser coupled with a monochromator to produce a wavelength tunable incident beam, which is weakly focused onto the device with a long-focal length (f = 200 mm) lens. Figure 3e,f shows the measured focusing intensity for the two polarizations at wavelengths ranging from 720 to 780 nm, demonstrating that the peaks can be resolved with a spectral resolution of 10 nm. In addition to the lateral shift, there is also a slight shift in the focal distance along the axial direction, resulting in a slight reduction in focusing intensity when deviating from the central wavelength (see details in Figure S5, Supporting Information). The spectral resolution of the device can be improved further by increasing the off-axis deflection angle or the device size. Our concept can readily extend to wavelength multiplexing multi-functionality, and an example of a metalens that can focus two sets of wavelengths to different off-axis positions is shown in Figure S6 (Supporting Information).

2.3. Radially Symmetric Large-Area High-Numerical-Aperture Metalens

In a second demonstration, we apply our concept to design radially symmetric metalenses for high-NA focusing. The design methodology is illustrated in **Figure** 4a and consists of partitioning the device into central and outer ring sections. In the central section, the NA is relatively low and conventional design methods based on local subwavelength-scale phase shifters[50] are sufficient. In the outer ring section, where the NA is high, we employ a radially symmetric arrangement of super-pixels, which are designed to scatter TE and TM polarized light with the desired angle and phase. While stitching discontinuities technically exist between adjacent deflectors due to the finite super-pixel lengths and widths, the resulting impact on performance is minimal for large zone sizes. The scalability of this approach makes it particularly suitable for constructing large-area, high-NA radially symmetric devices.

Figure 4a shows an example of the metalens designed using our approach. The lens has a diameter of 81 µm, comprises 450 nm-tall Si elliptical posts, and has an NA of 0.8. The boundary between the central and outer ring regions is located where the NA is 0.6, as indicated by a red dashed line. The focusing performance of the device is evaluated through full-wave simulations using MEEP, as depicted in Figure 4b top. The axial intensity distribution demonstrates excellent focusing cone with minimum unwanted diffraction. As a benchmark, we also design a conventional metalens with the same functionality utilizing subwavelength phase shifters based on local approximation (Figure 4b bottom). The metalens designed by our approach exhibits cleaner focusing and significantly less spurious diffraction around the edge of the lens. The focal spots at the focusing plane, as well as their 1D horizontal cut, are shown in Figure 4c,d, indicating that our proposed approach results in a more than 27% enhancement in focusing intensity compared to the conventional design. The focal spot of the optimized lens has a diffraction lim-

© 2024 Wiley-VCH GmbH

18638899, 0, Downloaded from https://onlinelibrary.wiley.com/doi/10.1002/lpor.202300988 by Stanford University, Wiley Online Library on [31/03/2024]. See the Terms and Conditions (https://onlinelibrary.wiley.com/terms-and-conditions) on Wiley Online Library for rules of use; OA articles are governed by the applicable Creative Commons License

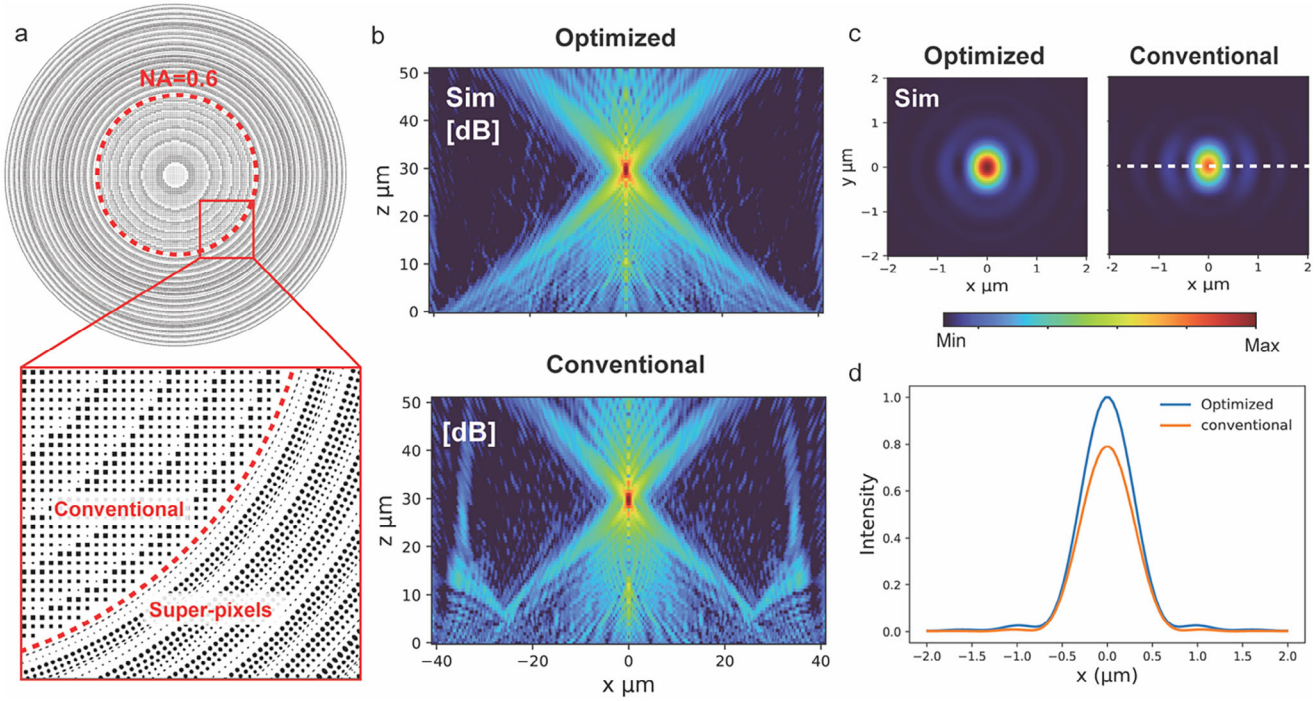

Figure 4. Radially symmetric large-area high-numerical-aperture metalens. a) Top view of a 81 µm lens. The device is partitioned into low numerical aperture (NA<0.6) and high numerical aperture (NA>0.6) regions, where each area is designed based on the conventional phase shifters and inverse-designed super-pixels, respectively. The inset shows an enlarged view of the boundary between the two design regions. b) Full-wave simulations of the axial intensity distributions by the optimized (top) and conventional (bottom) metalenses. c) Simulated focal spot profiles of the optimized (left) and conventional (right) metalenses. d) 1D horizontal cut of the focal spots (white dashed line in c).

ited full-width at half-maximums (FHHM) of 0.67 µm. The focusing efficiency is defined as the ratio between the transmitted power passing through a circular aperture at the focal plane and the total incident power on the lens. The metalens has a relative efficiency of 76%, and an absolute efficiency exceeding 66%. The design methology can be further extended to higher NAs, as demonstrated by the design of a metalens with an NA of 0.9 in Figure S7 (Supporting Information).

2.4. Metadevices for Generation and High-Numerical-Aperture Focusing of Vortex Beams

In a third demonstration, we show how super-pixels can serve as geometric phase elements to produce radial metalenses featuring a compact donut-shaped point spread function (PSF). Such beams have applications in particle trapping[51–53] and stimulated emission/depletion (STED) microscopy[54] and they are typically achieved by focusing a cylindrical vector beam[55] or vortex beam[56] through a high-NA microscope objective. With our inverse-designed super-pixels, we can combine the functions of vortex beam generation and high-NA focusing into a single device. By incorporating birefringence into the FOMs, we design a super-pixel to serve both as a half-wave plate and a beam deflector. A full-wave simulation of a representative super-pixel (**Figure** 5a) shows that the structure efficiently converts and deflects left-handed circularly polarized (LCP) light (Figure 5a left) into right-handed circularly polarized (RCP) light at a 30° angle (Figure 5a right), confirming that the super-pixel can simultaneously perform efficient large-angle deflection and conversion of circularly polarized light into its opposite handedness. By rotating the super-pixel, a geometric phase is introduced that equals twice the rotation angle for RCP or LCP light.

A schematic of the design concept for generating focused vortex beams is shown in Figure 5b. The deflector provides a gradient phase along the radial direction that focuses the incident beam, while the arrangement of deflectors in a radially symmetrical manner leads to the manifestation of a geometric phase response perpendicular to the deflection direction. By arranging the deflectors in a full circle, a total geometric phase response of 4π arises, producing a topological charge of $m = 2$ (see detailed elucidation on the topological charge in Section 8 and Figure S8, Supporting Information).

We employ the same hybrid design methodology that has been used for radially symmetrical metalenses to achieve high-NA focusing of a vortex beam. The designed device has a diameter of 108 µm, an NA of 0.8, and is partitioned into central and outer ring sections. The central section is designed using subwavelength-scale half-wave plates serving as local phase shifters, while the high NA outer ring section consists of super-pixel scatterers (see details of the designed structures and full-wave simulation in Section S9 and Figure S9, Supporting Information). The device is fabricated using electron beam lithography and reactive ion etching. Figure 5c shows the SEM images of the metalens in the center (NA<0.6, left) and outer region (NA>0.6, right). The device is measured upon LCP illumination using a

© 2024 Wiley-VCH GmbH

18638899, 0, Downloaded from https://onlinelibrary.wiley.com/doi/10.1002/lpor.202300988 by Stanford University, Wiley Online Library on [31/03/2024]. See the Terms and Conditions (https://onlinelibrary.wiley.com/terms-and-conditions) on Wiley Online Library for rules of use; OA articles are governed by the applicable Creative Commons License

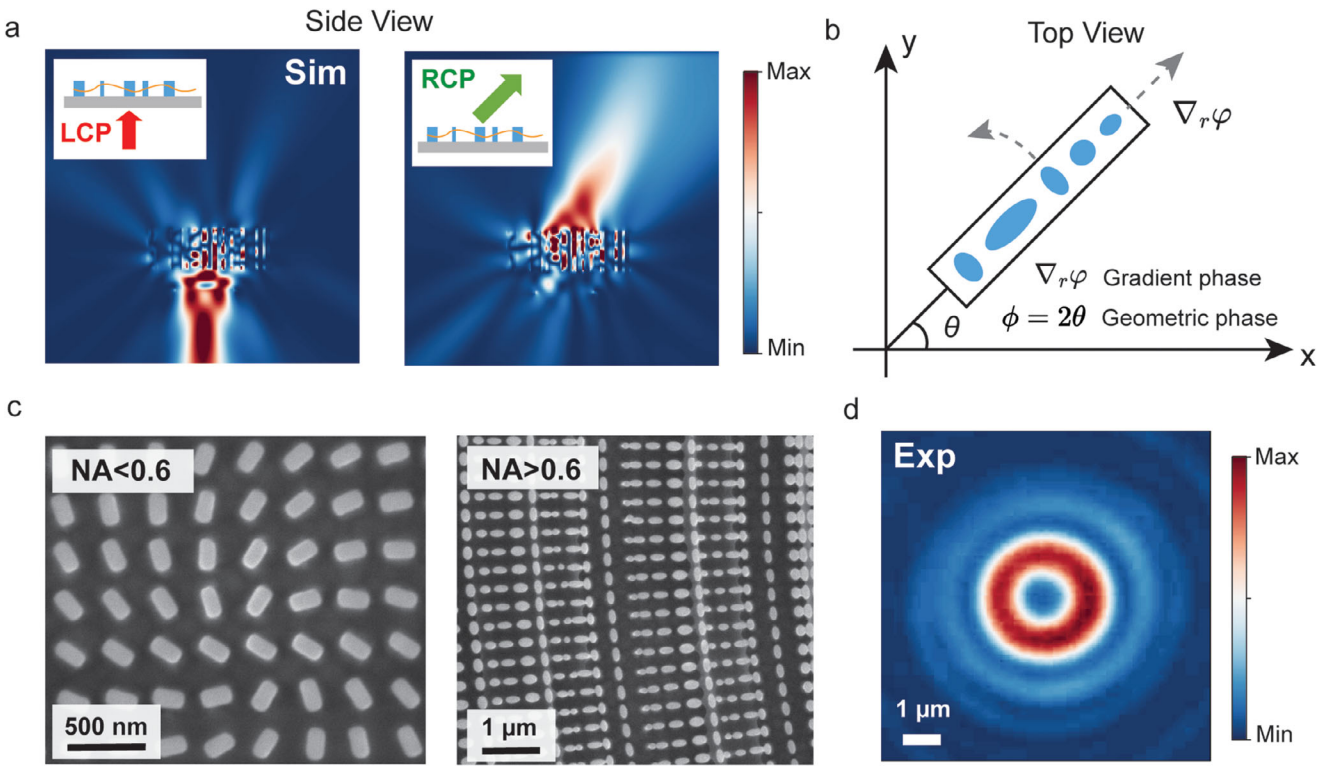

Figure 5. Metadevices for generation and focusing of vortex beams. a) Electric field distributions of an inverse-designed super-pixel capable of achieving polarization conversion and large-angle beam deflection. The device is illuminated by left-handed circularly polarized (LCP) light and outputs right-handed circularly polarized (RCP) light at the deflection angle of 30°. b) Schematic of the design concept for focusing of vortex beams. The aperiodic deflector can implement gradient phase and geometrical phase along the radial and azimuthal directions, respectively, enabling high-numerical-aperture focusing and the generation of spiral phase representing topological charges. c) SEM image of the device for high-numerical-aperture (NA = 0.8) focusing of vortex beams with a topological charge of $m = 2$. c) The low numerical aperture (NA<0.6) section is designed using conventional half-wave plate elements (left) while the high numerical aperture (NA>0.6) section is filled with radially patterned super-pixels (right). d) Point spread function (PSF) of the fabricated device.

linear polarizer and quarter-wave plate. The measured PSF at the focal plane illustrates a small ring with a well-defined dark center (Figure 5d).

3. Discussion

In summary, we demonstrate a design framework for realizing large-area freeform nanophotonic devices in which hard geometrical constraints such as minimum feature size and minimum gap size are incorporated through design space reparameterization. Our approach accounts for and utilizes full-wave interactions, including nonlocal interactions, between neighboring nanoscale elements. This results in the emergence of high-order hybridized modes, which enable super-pixels capable of supporting new scattering profiles compared to conventional means. To design the full-scale device, we sample the wavefront profile by a set of wavelength-scale segments, with each unit optimized as an inverse-designed deflector consisting of simple geometric layout. We apply our approach to achieve extreme wavefront control and demonstrate cylindrical metasurfaces supporting multifunctional super-dispersive focusing and high-NA radially symmetrical metalenses for diffraction limited focusing and generation of donut-shaped PSFs. This method has great potential for a wide range of applications, including microscopy, spectroscopy and structural light illumination[57] where large-angle beam deflection is critical for superior performance. Future advancements could include the development of faster electromagnetic solvers to accelerate full-wave simulations.[58–61] Furthermore, we can explore the integration of our devices with other optoelectronic and imaging systems to enable system-level applications, such as two-photon lithography,[62,63] LIDAR[64] and endoscopy[65] with enhanced performance and capabilities.

4. Experimental Section

Fabrication: The metasurfaces were defined on a polycrystalline Si wafer grown on a SiO_2 substrate using Low pressure chemical vapor deposition (LPCVD). An 80 nm thick hydrogen silsesquioxane (HSQ) was spin-coated on the Si substrate as the e-beam sensitive resist. Meanwhile, a thin layer of SURPRAS 3000 was spin coated for improving the surface adhesion between Si and HSQ. To help dissipate charge, a 200 nm thick Discharge H2O 2X was spin coated as the conduction layer. The HSQ patterns were then defined using electron beam lithography. Post-development hard bake was performed at 420 C to strengthen the crosslinking in HSQ. Finally, the Si nanorods are etched by reactive ion etching using a mixture of hydrogen bromide and chlorine.

 © 2024 Wiley-VCH GmbH

18638899, 0, Downloaded from https://onlinelibrary.wiley.com/doi/10.1002/lpor.202300988 by Stanford University, Wiley Online Library on [31/03/2024]. See the Terms and Conditions (https://onlinelibrary.wiley.com/terms-and-conditions) on Wiley Online Library for rules of use; OA articles are governed by the applicable Creative Commons License

Supporting Information

Supporting Information is available from the Wiley Online Library or from the author.

Acknowledgements

This work was supported by the Department of Energy and Lawrence Livermore National Lab Contract No. DE-AC52-07NA27344, the Office of Naval Research under Award Number N00014-20-1-2105, and the National Science Foundation under Award 2103301.

Conflict of Interest

The authors declare no conflict of interest.

Author Contributions

Y.Z. and C.M. contributed equally to this work. Y.Z. performed the design, modeling, and theoretical analysis. Y.Z., E.G., and M.C. formulated the design algorithms. C.M. fabricated the samples and performed the measurements. Y.Z. and J.F. wrote the manuscript with input from all of the authors. The project was supervised by J.F.

Data Availability Statement

The data that support the findings of this study are available from the corresponding author upon reasonable request.

Keywords

freeform metasurfaces, High numerical aperture, Inverse design, topology optimization

Received: October 3, 2023
Revised: December 27, 2023
Published online:

[1] Q. Cheng, M. Bahadori, M. Glick, S. Rumley, K. Bergman, *Optica* **2018**, *5*, 1354.
[2] A. Alù, N. Engheta, Performing Methematical Operations with Metamaterials, Science **2014**, *343*, 160.
[3] Y. Zhou, H. Zheng, I. I. Kravchenko, J. Valentine, *Nat. Photonics* **2020**, *14*, 316.
[4] Y. Zhou, I. I. Kravchenko, H. Wang, H. Zheng, G. Gu, J. Valentine, *Light Sci Appl* **2019**, *8*, 80.
[5] D. Lin, A. L. Holsteen, E. Maguid, G. Wetzstein, P. G. Kik, E. Hasman, M. L. Brongersma, *Nano Lett.* **2016**, *16*, 7671.
[6] M. Khorasaninejad, W. T. Chen, R. C. Devlin, J. Oh, A. Y. Zhu, F. Capasso, *Science* **2016**, *352*, 1190.
[7] W. T. Chen, A. Y. Zhu, V. Sanjeev, M. Khorasaninejad, Z. Shi, E. Lee, F. Capasso, *Nat. Nanotechnol.* **2018**, *13*, 220.
[8] Y. Zhou, I. I. Kravchenko, H. Wang, J. R. Nolen, G. Gu, J. Valentine, *Nano Lett.* **2018**, *18*, 7529.
[9] H. Zheng, Y. Zhou, C. F. Ugwu, A. Du, I. I. Kravchenko, J. G. Valentine, *ACS Photonics* **2021**, *8*, 1824.
[10] E. Arbabi, S. M. Kamali, A. Arbabi, A. Faraon, *ACS Photonics* **2018**, *5*, 3132.
[11] N. A. Rubin, G. D'Aversa, P. Chevalier, Z. Shi, W. T. Chen, F. Capasso, *Science* **2019**, *364*, eaax1839.
[12] B. A. Slovick, Y. Zhou, Z. G. Yu, I. I. Kravchenko, D. P. Briggs, P. Moitra, S. Krishnamurthy, J. Valentine, *Philos Trans A Math Phys Eng Sci* **2017**, *375*, 20160072.
[13] L. Wang, S. Kruk, H. Tang, T. Li, I. Kravchenko, D. N. Neshev, Y. S. Kivshar, *Optica* **2016**, *3*, 1504.
[14] G. Zheng, H. Mühlenbernd, M. Kenney, G. Li, T. Zentgraf, S. Zhang, *Nat. Nanotechnol.* **2015**, *10*, 308.
[15] K. Shastri, F. Monticone, *Nat. Photonics* **2023**, *17*, 36.
[16] A. Overvig, A. D. N. M Alù, *Laser Photonics Rev.* **2022**, *16*, 2100633.
[17] Y. Zhou, S. Guo, A. C. Overvig, A. M. N. M Alù, *Nano Lett.* **2023**, *23*, 6768.
[18] A. Overvig, A. Alù, *Adv. Photonics* **2021**, *3*, 026002.
[19] A. Ji, J.-H. Song, Q. Li, F. Xu, C.-T. Tsai, R. C. Tiberio, B. Cui, P. Lalanne, P. G. Kik, D. A. B. Miller, M. L. Brongersma, *Nat. Commun.* **2022**, *13*, 7848.
[20] X. Wang, H. Wang, J. Wang, X. Liu, H. Hao, Y. S. Tan, Y. Zhang, H. Zhang, X. Ding, W. Zhao, Y. Wang, Z. Lu, J. Liu, J. K. W. Yang, J. Tan, H. Li, C.-W. Qiu, G. Hu, X. Ding, *Nat. Commun.* **2023**, *14*, 2063.
[21] L. Zhang, S. Chang, X. Chen, Y. Ding, M. T. Rahman, Y. Duan, M. Stephen, X. Ni, *Nano Lett.* **2022**, *23*, 51.
[22] S. Pinilla, J. E. Fröch, S. R. Miri Rostami, V. Katkovnik, I. Shevkunov, A. Majumdar, K. Egiazarian, *Sci. Adv.* **2023**, *9*, eadg7297.
[23] C. M. Lalau-Keraly, S. Bhargava, O. D. Miller, E. Yablonovitch, *Opt. Express* **2013**, *21*, 21693.
[24] S. Molesky, Z. Lin, A. Y. Piggott, W. Jin, J. Vuckovic, A. W. Rodriguez, *Nat. Photonics* **2018**, *12*, 659.
[25] D. Sell, J. Yang, S. Doshay, R. Yang, J. A. Fan, *Nano Lett.* **2017**, *17*, 3752.
[26] D. Sell, J. Yang, S. Doshay, J. A. Fan, *Adv. Opt. Mater.* **2017**, *5*, 1700645.
[27] Z. Shi, A. Y. Zhu, Z. Li, Y.-W. Huang, W. T. Chen, C.-W. Qiu, F. Capasso, *Sci. Adv.* **2020**, *6*, eaba3367.
[28] Z. Lin, B. Groever, F. Capasso, A. W. Rodriguez, M. Lončar, *Phys. Rev. Appl.* **2018**, *9*, 044030.
[29] M. Mansouree, A. McClung, S. Samudrala, A. Arbabi, *ACS Photonics* **2021**, *8*, 455.
[30] T. Phan, D. Sell, E. W. Wang, S. Doshay, K. Edee, J. Yang, J. A. Fan, *Light Sci Appl* **2019**, *8*, 48.
[31] D.i Sang, M. Xu, M. Pu, F. Zhang, Y. Guo, X. Li, X. Ma, Y. Fu, X. Luo, *Laser Photon. Rev.* **2022**, *16*, 2200265.
[32] M. Xu, Q. He, M. Pu, F. Zhang, L. Li, D.i Sang, Y. Guo, R. Zhang, X. Li, X. Ma, X. Luo, *Adv. Mater.* **2022**, *34*, 2108709.
[33] G. Roberts, C. Ballew, T. Zheng, J. C. Garcia, S. Camayd-Muñoz, P. W. C. Hon, A. Faraon, *Nat. Commun.* **2023**, *14*, 2768.
[34] B. Shen, P. Wang, R. Polson, R. Menon, *Nat. Photonics* **2015**, *9*, 378.
[35] A. Y. Piggott, J. Lu, K. G. Lagoudakis, J. Petykiewicz, T. M. Babinec, J. Vuckovic, *Nat. Photonics* **2015**, *9*, 374.
[36] E. W. Wang, D. Sell, T. Phan, J. A. Fan, *Opt. Mater. Express* **2019**, *9*, 469.
[37] X. Qian, M. Yuan, E. Khoram, Z. Yu, *Opt. Express* **2020**, *28*, 7060.
[38] A. M. Hammond, A. Oskooi, S. G. Johnson, S. E. Ralph, *Opt. Express* **2021**, *29*, 23916.
[39] J. S. Jensen, O. Sigmund, *JOSA B* **2005**, *22*, 1191.
[40] M. Zhou, B. S. Lazarov, F. Wang, O. Sigmund, *Comput Methods Appl Mech Eng* **2015**, *293*, 266.
[41] D. Vercruysse, N. V. Sapra, L. Su, R. Trivedi, J. Vučković, *Sci. Rep.* **2019**, *9*, 8999.
[42] M. Mansouree, H. Kwon, E. Arbabi, A. McClung, A. Faraon, A. Arbabi, *Optica* **2020**, *7*, 77.
[43] E. Gershnabel, M. Chen, C. Mao, E. W. Wang, P. Lalanne, J. A. Fan, *ACS Photonics* **2023**, *10*, 815.
[44] M. Chen, J. Jiang, J. A. Fan, *ACS Photonics* **2020**, *7*, 3141.

 © 2024 Wiley-VCH GmbH

18638899, 0, Downloaded from https://onlinelibrary.wiley.com/doi/10.1002/lpor.202300988 by Stanford University, Wiley Online Library on [31/03/2024]. See the Terms and Conditions (https://onlinelibrary.wiley.com/terms-and-conditions) on Wiley Online Library for rules of use; OA articles are governed by the applicable Creative Commons License

[45] M. Khorasaninejad, W. T. Chen, J. Oh, F. Capasso, *Nano Lett.* **2016**, *16*, 3732.
[46] F. Yesilkoy, E. R. Arvelo, Y. Jahani, M. Liu, A. Tittl, V. Cevher, Y. Kivshar, H. Altug, *Nat. Photonics* **2019**, *13*, 390.
[47] A. Arbabi, Y. Horie, M. Bagheri, A. Faraon, *Nat. Nanotechnol.* **2015**, *10*, 937.
[48] J. Zhou, H. Qian, G. Hu, H. Luo, S. Wen, Z. Liu, *ACS Nano* **2018**, *12*, 82.
[49] A. F. Oskooi, D. Roundy, M. Ibanescu, P. Bermel, J. D. Joannopoulos, S. G. Johnson, *Comput. Phys. Commun.* **2010**, *181*, 687.
[50] A. Arbabi, Y. Horie, A. J. Ball, M. Bagheri, A. Faraon, *Nat. Commun.* **2015**, *6*, 7069.
[51] L. Paterson, M. P. MacDonald, J. Arlt, W. Sibbett, P. E. Bryant, K. Dholakia, *Science* **2001**, *292*, 912.
[52] A. Ashkin, *Biophys. J.* **1992**, *61*, 569.
[53] K. T. Gahagan, G. A. J. Swartzlander, *Opt. Lett.* **1996**, *21*, 827.
[54] M. Dyba, S. W. Hell, *Phys. Rev. Lett.* **2002**, *88*, 163901.
[55] Q. Zhan, *Adv. Opt. Photonics* **2009**, *1*, 1.
[56] D. Ganic, X. Gan, M. Gu, *Opt. Express* **2003**, *11*, 2747.
[57] G. Kim, Y. Kim, J. Yun, S.-W. Moon, S. Kim, J. Kim, J. Park, T. Badloe, I. Kim, J. Rho, *Nat. Commun.* **2022**, *13*, 5920.
[58] M. Chen, R. Lupoiu, C. Mao, D.-H. Huang, J. Jiang, P. Lalanne, J. A. Fan, *ACS Photonics* **2022**, *9*, 3110.
[59] Y. Augenstein, T. Repän, C. Rockstuhl, *ACS Photonics* **2023**, *10*, 1547.
[60] M. Zhelyeznyakov, J. Froch, A. Wirth-Singh, J. Noh, J. Rho, S. Brunton, A. Majumdar, *Commun. Eng.* **2023**, *2*, 60.
[61] Z. Li, R. Pestourie, J.-S. Park, Y.-W. Huang, S. G. Johnson, F. Capasso, *Nat. Commun.* **2022**, *13*, 2409.
[62] M. Farsari, B. N. Chichkov, *Nat. Photonics* **2009**, *3*, 450.
[63] T. Gissibl, S. Thiele, A. Herkommer, H. Giessen, *Nat. Photonics* **2016**, *10*, 554.
[64] I. Kim, R. J. Martins, J. Jang, T. Badloe, S. Khadir, H.o-Y. Jung, H. Kim, J. Kim, P. Genevet, J. Rho, *Nat. Nanotechnol.* **2021**, *16*, 508.
[65] H. Pahlevaninezhad, M. Khorasaninejad, Y.-W. Huang, Z. Shi, L. P. Hariri, D. C. Adams, V. Ding, A. Zhu, C.-W. Qiu, F. Capasso, M. J. Suter, *Nat. Photonics* **2018**, *12*, 540.

© 2024 Wiley-VCH GmbH

18638899, 0, Downloaded from https://onlinelibrary.wiley.com/doi/10.1002/lpor.202300988 by Stanford University, Wiley Online Library on [31/03/2024]. See the Terms and Conditions (https://onlinelibrary.wiley.com/terms-and-conditions) on Wiley Online Library for rules of use; OA articles are governed by the applicable Creative Commons License